Boundary-Layer Meteorol (2011) 141:393–414
DOI 10.1007/s10546-011-9641-1

ARTICLE

Turbulent Transfer Between Street Canyons and the Overlying Atmospheric Boundary Layer

Pietro Salizzoni · Massimo Marro · Lionel Soulhac · Nathalie Grosjean · Richard J. Perkins

Received: 20 December 2010 / Accepted: 14 July 2011 / Published online: 3 August 2011
© Springer Science+Business Media B.V. 2011

Abstract The turbulent exchange of momentum between a two-dimensional cavity and the overlying boundary layer has been studied experimentally, using hot-wire anemometry and particle image velocimetry (PIV). Conditions within the boundary layer were varied by changing the width of the canyons upstream of the test canyon, whilst maintaining the square geometry of the test canyon. The results show that turbulent transfer is due to the coupling between the instabilities generated in the shear layer above the canyons and the turbulent structures in the oncoming boundary layer. As a result, there is no single, unique velocity scale that correctly characterizes all the processes involved in the turbulent exchange of momentum across the boundary layer. Similarly, there is no single velocity scale that can characterize the different properties of the turbulent flow within the canyon, which depends strongly on the way in which turbulence from the outer flow is entrained into the cavity and carried round by the mean flow. The results from this study will be useful in developing simple parametrizations for momentum exchange in the urban canopy, in situations where the street geometry consists principally of relatively long, uniform streets arranged in grid-like patterns; they are unlikely to be applicable to sparse geometries composed of isolated three-dimensional obstacles.

Keywords Atmospheric turbulence · Momentum transfer · Shear-layer flow · Street canyon · Urban canopy

1 Introduction

Turbulent transfer between the atmosphere and an urban or vegetation canopy determines the concentration of a pollutant in the canopy and the characteristics of the boundary layer

P. Salizzoni (✉) · M. Marro · L. Soulhac · N. Grosjean · R. J. Perkins
Laboratoire de Mécanique des Fluides et d'Acoustique, University of Lyon,
CNRS UMR 5509 Ecole Centrale de Lyon, INSA Lyon, Université Claude Bernard,
36, avenue Guy de Collongue, 69134 Ecully, France
e-mail: pietro.salizzoni@polito.it

aloft. Consequently, several studies in recent years have been devoted to the analysis of flow and dispersion in plant canopies over flat and hilly terrain (Finnigan 1985, 2000; Kaimal and Finnigan 1994; Poggi and Katul 2007) or urban canopies, composed of groups of obstacles with varying geometries and spacing (Soulhac 2000; Coceal and Belcher 2004; Belcher 2005; Coceal et al. 2006, 2007; Harman and Belcher 2006; Hamlyn et al. 2007; Garbero et al. 2010).

Generally the aim of these studies has been to identify the statistical properties of the velocity field that influence the transfer of momentum, mass and heat between the canopy and the atmosphere. Most of the studies focus on the relationship between the turbulent transfer and parameters that describe the geometry of the canopy elements. The turbulent transfer is then usually expressed as a function of porosity factors related to the building density for cities (Grimmond and Oke 1999), or to the leaf area index for forests (Kaimal and Finnigan 1994).

However, as far as we are aware, only a few studies have investigated the influence of the structure of the external boundary-layer on the flow in the canopy. Kim and Baik (2003) used numerical simulations to investigate the effects of inflow turbulence in an urban canyon flow; Louka et al. (2000) focused on the coupling between the recirculating region in the urban canyon and the boundary-layer flow aloft; and Soulhac (2000) and Caton et al. (2003) developed similar analytical models describing the canyon-atmosphere transfer as a function of the turbulence intensity of the external flow.

Our study focusses on urban canopy flow and its interaction with the overlying atmospheric boundary-layer flow, and complements the results presented by Salizzoni et al. (2009a) for street-canyon ventilation. The investigation is limited to the case of a simplified urban geometry, consisting of a series of two-dimensional street canyons. This is a drastic simplification of real urban geometry, but it is necessary in order to clarify the basic governing mechanisms of the phenomenon (Harman and Belcher 2006; Simoëns et al. 2007; Huq et al. 2007). The experimental configuration was designed to simulate a neutral atmospheric boundary layer above the street canyons, with a boundary-layer depth approximately ten times the canyon height. This is an important feature that makes the experiments discussed here different from those presented in other studies dealing with urban-canyon flows (Caton et al. 2003; Simoëns et al. 2007; Huq et al. 2007).

Much of the previous work on urban canopy has focused on the role of local conditions in determining flow and dispersion, and rather less attention has been paid to the influence of the incoming boundary layer. But real urban surfaces are a complicated mixture of obstacles of different sizes and orientations, with significant variations in geometric characteristics both at the scale of the street and at the scale of the district. So, in general, the external flow will not be in equilibrium with the conditions imposed by the local surface geometry. The principal objective of our work is to study how conditions in the external flow affect flow within an urban-street canyon, and how they influence exchanges between the cavity and the external flow. The aim is then to derive scaling relationships for these properties, which take into account the characteristics of the external flow, and which can be incorporated into operational urban air-quality models. In particular, the results from this study (and others) will be used to improve the parametrization of exchanges within the urban canopy in the operational model SIRANE (Soulhac et al. 2003).

In Sect. 2 we outline the theoretical arguments used to interpret the results, with details of the experimental set-up and techniques given in Sect. 3; the experimental results are presented and discussed in Sect. 4 and conclusions are drawn in Sect. 5.

2 Transfer Mechanism

It is convenient to divide the flow domain into three main regions—the external boundary layer, the cavity and the shear layer at the interface between them. The external flow (Salizzoni et al. 2008) behaves essentially as a classical rough wall turbulent boundary layer (Jimènez 2004) within which we can identify three distinct regions—the outer region, the inner region and the roughness sub-layer, extending from the canyon top to the lower limit of the inertial layer (Raupach et al. 1991). The flow within the cavity takes the form of a recirculating eddy driven by the outer flow. The high shear levels at the top of the canyon generate a Kelvin–Helmholtz type instability in the layer (e.g. Fig. 1) leading to the formation of large-scale spanwise-coherent vortices that play a particularly important role in mass and momentum transfer. So, in order to parametrize the mass and momentum transfer between the cavity and the external flow, it is particularly important to understand the interaction between the flow in the shear layer and the flows in the regions on either side (Huq et al. 2007).

One problem in particular is to evaluate whether the dynamics of the shear layer depend only on the local production of turbulence or if they also depend on the dynamics of the external boundary layer. In the former case the cavity flow would be driven directly by the dynamics of the shear layer, which 'shelters' the cavity flow from the atmospheric turbulence. In the latter case the flow within the cavity must also be influenced by the structure of the atmospheric turbulence.

To examine this question we have focused our attention on the influence of the dynamical conditions of the flow in the boundary layer on the flow in a canyon with a fixed square geometry (aspect ratio ∼1). It follows from the previous discussion that there are two possible velocity scales for the flows. The first is ΔU—the mean velocity difference across the shear layer—and is related to the local generation of turbulence within the shear layer. The second is the friction velocity of the external flow, referred to as u_*, which is assumed to be the only relevant velocity scale for the boundary-layer turbulence. We have then analyzed the experimental data to test three hypotheses:

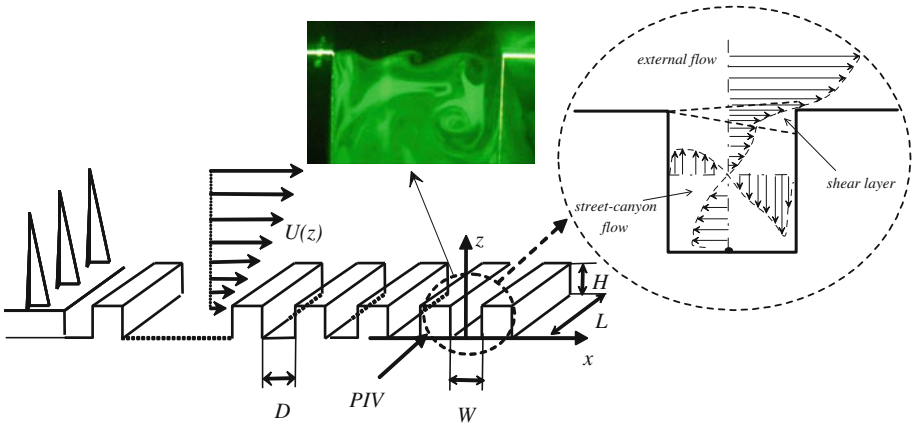

Fig. 1 Experimental set-up. The *dotted circle* indicates the canyon within which PIV measurements were performed. The photograph shows a flow visualization of the Kelvin–Helmholtz instability that develops at the top of the street canyon

1. The flow within the canyon depends only on the shear-layer dynamics, i.e. on the turbulent structures arising and developing within it. All velocities within the cavity and within the shear layer should therefore scale only on ΔU, the mean velocity difference across the shear layer:

$$\frac{\overline{u}}{\Delta U} = \beta_1, \tag{1a}$$

$$\frac{\overline{u'w'}}{\Delta U^2} = \beta_2, \tag{1b}$$

$$\frac{q^2/2}{\Delta U^2} = \beta_3 \tag{1c}$$

   etc., where $\beta_1, \beta_2, \beta_3$ are invariant form functions, $\overline{u}$ is the longitudinal component of the mean velocity, $\overline{u'w'}$ is the Reynolds stress and $q^2/2$ is the turbulent kinetic energy (t.k.e.).
2. The dynamics of the flow within the canyon depend only on the dynamics of the external boundary-layer flow. All velocities within the cavity and within the shear layer therefore scale on the friction velocity u_*. The functions $\beta_1, \beta_2, \beta_3$ could depend on the structure of the external flow so we can therefore write

$$\frac{\overline{u}}{u_*} = \beta_1\left(\frac{L_{ww}}{W}\right), \tag{2a}$$

$$\frac{\overline{u'w'}}{u_*^2} = \beta_2\left(\frac{L_{ww}}{W}\right), \tag{2b}$$

$$\frac{q^2/2}{u_*^2} = \beta_3\left(\frac{L_{ww}}{W}\right), \tag{2c}$$

   etc., where W is the canyon width (Fig. 1) and L_{ww} is a measure of the integral length scale of the external boundary-layer flow, which we expect to be linked to the depth of the roughness sub-layer. It is worth noting that L_{ww} varies significantly both longitudinally and vertically in the lowest part of the boundary layer so it is difficult to define a representative value for this length scale, characteristic of the flow throughout the region. This is discussed in detail in Sect. 4.1.
3. The dynamics of the flow within the canyon depend on both the turbulence generated within the shear layer and the turbulent eddies in the external flow that are entrained by the shear layer and injected into the cavity. In this case the form functions $\beta_1, \beta_2, \beta_3$ can be written:

$$\frac{\overline{u}}{\Delta U} = \beta_1\left(\frac{u_*}{\Delta U}, \frac{L_{ww}}{W}\right), \tag{3a}$$

$$\frac{\overline{u'w'}}{\Delta U^2} = \beta_2\left(\frac{u_*}{\Delta U}, \frac{L_{ww}}{W}\right), \tag{3b}$$

$$\frac{q^2/2}{\Delta U^2} = \beta_3\left(\frac{u_*}{\Delta U}, \frac{L_{ww}}{W}\right), \tag{3c}$$

etc. The two velocity scales u_* and ΔU are not independent of each other, in the sense that a change in u_* can (and in most circumstances, will) lead to a change in ΔU. But the relationship between the two is not simple since it depends on other, independent, parameters,

Table 1 External boundary-layer and shear-layer flow parameters in the four configurations (see Fig. 1)

Config.	H/W	H/D	u_* (m s^{-1})	z_0 (mm)	d (mm)	z_*/H	ΔU (m s^{-1})	$\Delta U/u_*$
A	1	1	0.33	0.3	57	7/6	1.35	4.09
B	1	2/3	0.36	0.6	55	8/6	1.18	3.27
C	1	1/2	0.41	1.7	52	2	1.02	2.48
D	1	1/3	0.46	2.7	46	2	0.91	1.98

The boundary-layer depth δ and the free stream velocity U_∞ at the top of the boundary layer do not vary between the configurations and are equal to 0.6 m and 6.75 m s^{-1} respectively

including the aspect ratio of the cavity, the roughness of the cavity walls and the roughness of the surface upstream of the cavity. In these experiments the conditions in the cavity do not change, but the upstream the conditions do change from one configuration to another. As a result, u_* varies, even though U_∞ is maintained constant, and as can be seen in Table 1, an increase in u_* results in a decrease in ΔU. The exact nature of the relationship between u_* and ΔU certainly deserves further study, since it will play an important role in determining exchanges within the urban canopy. However, as discussed in Sect. 4.2, it should be remembered that the mixing layer at the top of the canopy is not exactly the same as the standard mixing layer, and that ΔU is therefore not exactly the same as that usually used to characterize laboratory mixing layers.

For completeness, we also present the data normalized with U_∞, the velocity at the top of the boundary layer. However, since U_∞ is identical in all four configurations, these profiles are directly representative of the raw data.

3 Experimental Details

3.1 Experimental Configuration

The experiments were performed in a recirculating wind tunnel at the Laboratoire de Mécanique des Fluides et d'Acoustique at the Ecole Centrale de Lyon. The test section of the wind tunnel is 8 m long, 1 m high and 0.7 m wide. To generate a boundary layer with characteristics similar to those of an atmospheric boundary layer, we used a combination of spires at the entrance to the test section and roughness blocks on the floor of the tunnel, as originally proposed by Irwin (1981). In these experiments three spires with a height of 0.5 m were used. We have simulated an idealized street geometry consisting of a sequence of two-dimensional (2D) parallel canyons, formed by a set of square section bars (60 mm $\times$ 60 mm) placed normal to the flow, as shown in Fig. 1. The bars spanned the entire width of the test section, so that the ratio L/H of length L to height H was approximately 12. The experiments were performed for a constant external velocity $U_\infty \approx 6.75\,\mathrm{m\,s^{-1}}$. The velocity profiles in the external flow were measured downstream of the entry to the test section at a distance equal to about 12 times the height of the vortex generators. This distance provided a sufficient fetch to guarantee that the boundary-layer flow could reach an equilibrium condition (Salizzoni et al. 2008).

The influence of the upstream conditions was studied by keeping the canyon aspect ratio constant ($H/W = 1$) and varying the geometry (H/D) of the upstream canyons. This can be also seen as a sudden roughness change at the position of the measurement section in the

instrumented canyon. This arrangement allowed us to produce different incoming velocity profiles driving the flow within a cavity with fixed geometry. Details of the four configurations studied are given in Table 1.

3.2 Experimental Techniques

We employed two different techniques to measure velocities—hot-wire anemometry (HWA) in the external boundary-layer flow and particle image velocimetry (PIV) within the cavity. In the external flow ($H < z < \delta$), velocities were measured by HWA, using an X-probe functioning as a constant temperature anemometer, with a sampling frequency of 5000 Hz. Details of the statistical properties of the velocity field are provided in Salizzoni et al. (2008). Velocities within the cavity and in the lowest part of the boundary-layer flow were measured using PIV. Two coupled YAG laser sources provided pairs of laser pulses at a syncronized frequency of about 8 Hz. The visualization light sheet measured 1 mm in width and the flow was seeded with micron-sized droplets produced by a smoke generator.

The observation field measured approximately 120×120 mm^2, and this was filmed at a resolution of $1{,}280 \times 1{,}024$ pixels. The interrogation window was fixed at 16×16 pixels, corresponding to an averaging area of about 1.1 mm $\times$ 0.9 mm. The interrogation windows overlapped by 50 % so that, in total, each pair of images yielded a set of 240×240 velocity vectors. In each configuration the velocity field was sampled 1,000 times at a frequency of 4 Hz and these velocity fields were used to compute ensemble-averaged statistics.

By patching together the results from the different overlapping interrogation windows we obtained velocity measurements in the domain $-3/2 < x/H < 3/2, 0 < z/H < 5/2$. The PIV measurements overlap with the hot-wire anemometer data in the region $H < z < 2H$. Vertical profiles of mean velocity and turbulent quantities, measured at the centre of the cavity and obtained using both HWA and PIV are shown superposed in Fig. 2. For all three quantities (U/U_∞, $\frac{1}{2}q^2/U_\infty^2$, $-\overline{u'w'}/U_\infty^2$) the two datasets are in reasonable agreement in the overlap region; the agreement is closest for the mean velocity (Fig. 2a) and for the t.k.e. (Fig. 2b) and least satisfactory for the Reynolds stress (Fig. 2c). For this variable the PIV profiles show more scatter and provide higher values, and in agreement with previous experimental results (Stanislas et al. 1998).

The analysis of the flow in the shear layer requires an estimate of the gradient of averaged velocities. The error in the evaluation of the spatial derivatives clearly depends on the experimental error, given by a systematic error (bias) and a random error (root-mean square, r.m.s.). For a single point in the interrogation window, we may assume that if the flow is locally homogeneous, then so will be the bias. Conversely, the random error is likely to vary

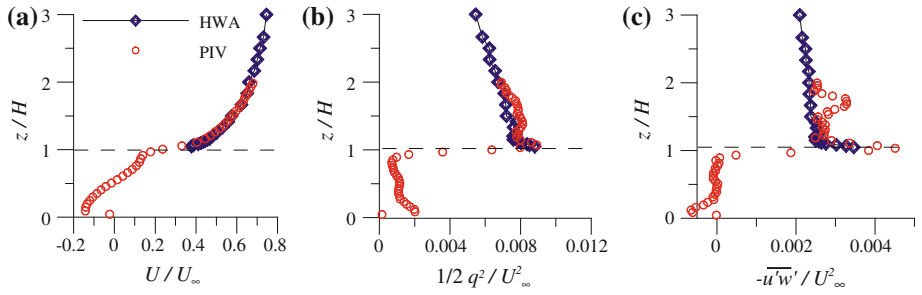

Fig. 2 Comparison between PIV data ($0 < z < 2H$) and HWA data ($H < z < 3H$) for configuration A

from one measurement point to the next, and this can have a significant effect on the estimation of the velocity gradients. To reduce this source of error we applied a low-pass filter to the velocity data (Fouras and Soria 1998; Castelain 2006), by interpolating the velocity field using a second-order polynomial function of x and y:

$$u(x, y) = a_1x^2y^2 + a_2x^2y + a_3xy^2 + a_4xy + a_5x^2 + a_6y^2 + a_7x + a_8y + a_9, \quad (4)$$

$$v(x, y) = b_1x^2y^2 + b_2x^2y + b_3xy^2 + b_4xy + b_5x^2 + b_6y^2 + b_7x + b_8y + b_9. \quad (5)$$

The 18 coefficients were evaluated for each point in the domain, using a least square minimization procedure over the surrounding 24 points.

4 Experimental Results

4.1 External Flow

The influence of the external flow was studied by varying the aspect ratio H/D of the cavities upstream of the test cavity (Fig. 1), for which the height (H) to width (W) ratio was kept constant ($H/W = 1$). Overall, four different upstream configurations have been analyzed: configurations A and B correspond to skimming flow, and configurations C and D to wake interference flow.[1] The incident wind profile depends on the aspect ratio of the upwind canyons; as the aspect ratio decreases, from configuration A to configuration D, the mean velocities decrease (Fig. 3a) whereas the Reynolds stresses and the t.k.e. increase (Fig. 3b, c).

As discussed in Salizzoni et al. (2008), the velocity profiles above the upstream obstacles for the four different configurations are similar, since they can be collapsed in a large part of the domain if the scaling parameters are chosen appropriately. These are the friction velocity u_*, the boundary-layer height δ, the roughness length z_0 and the displacement height d. Of these length scales, the first represents an imposed external length scale, whilst the other two depend on the surface roughness (characterized in these experiments by the ratio H/D) and can be obtained by fitting a logarithmic profile to the measurements in the inertial region:

$$\frac{\overline{u}(z)}{u_*} = \frac{1}{\kappa} \ln \frac{(z - d)}{z_0}. \quad (6)$$

The values of these parameters for all four configurations are given in Table 1, together with the values for the lower limit of the inertial region z_*, which we refer to here as the 'blending height', below which the flow dynamics are directly influenced by the wake of each obstacle and so cannot be considered homogeneous. Details of the method used to estimate the parameters in Table 1 (with the associated errors) are given in Salizzoni et al. (2008).

The different velocity profiles cannot, however, be considered rigorously similar (Salizzoni et al. 2009b, 2010) over their full extent, since the depth of the roughness sub-layer, and therefore the ratio z_*/H, varies from one configuration to the other. This layer is thinnest ($z_*/H \approx 1.2$) for skimming flow configurations and increases as the obstacle spacing increases (values of z_* are provided in Table 1); however, once the flow regime changes from skimming to wake interference, the blending height increases significantly. An indirect confirmation of the link between the depth of the roughness sub-layer and the size of the largest vortices (i.e. the local integral length scale) in the lowest part of the boundary-layer

[1] The upstream conditions for configurations A and C are identical to those for configurations 1a and 3a respectively, as described in Salizzoni et al. (2008).

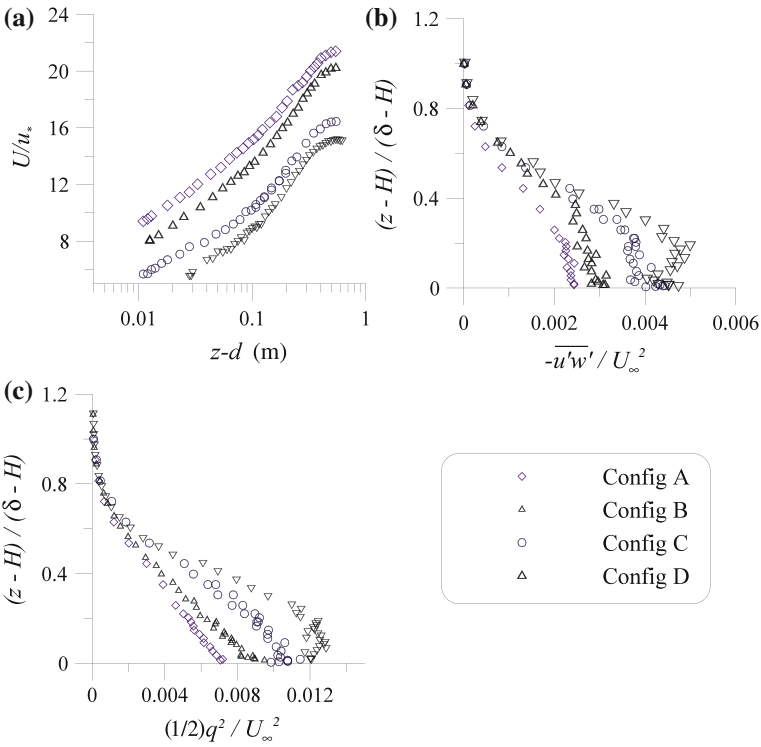

Fig. 3 External flow conditions. Velocity profiles measured with HWA at the centre of the cavity, i.e. at $x = 0$ (see Fig. 1)

flow was provided by numerical simulations of the dispersion of a passive scalar (Salizzoni et al. 2009b).

To provide more information on the spatial structure of the turbulence we have computed the two-point velocity correlations throughout the domain. We focus here on the structure function of the vertical velocity component R_{ww}, which is defined as:

$$R_{\mathrm{ww}}(\mathbf{x_0}, \mathbf{r}) = \frac{\overline{w'(\mathbf{x_0})w'(\mathbf{x_0}+\mathbf{r})}}{[\sigma_{\mathrm{w}}(\mathbf{x_0})\sigma_{\mathrm{w}}(\mathbf{x_0}+\mathbf{r})]} \tag{7}$$

where $\mathbf{x_0}$ is any point in the domain, $\mathbf{r}$ is a displacement relative to $\mathbf{x_0}$ and the averaging is performed over time. The integral of the structure function over $\mathbf{r}$ gives a length scale—the integral length scale—representative of the distance over which the velocities are correlated. We focus here on the integral length scale L_{ww}, related to the vertical velocity, since we are mainly interested in momentum transfer in the vertical direction. The structure functions R_{ww} computed for configuration A and configuration C at the position $x/H = 0, z/H = 4/3$ (Fig. 4), provide further evidence of the change in length scale. The plot shows that the integral length scales L_{ww} for the vertical velocity component are greater for configuration C than for configuration A.

To quantify these differences we consider the variations in R_{ww} as a function of distance (z) from the base of the cavity along a vertical line passing through the centre of the cavity. To calculate L_{ww} at each position we assume that the velocity structure function can be

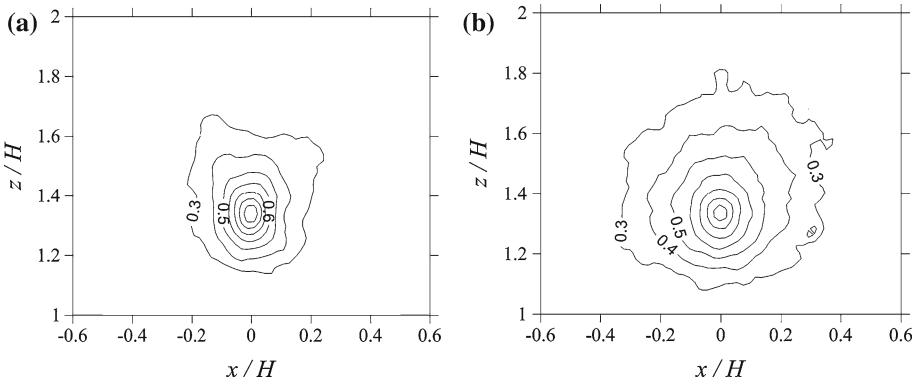

Fig. 4 Structure functions of the vertical velocity R_{ww} computed at $z = (4/3)H$ in the external flow in **a** skimming flow (configuration A) and **b** wake interference regime (configuration C)

modelled as an exponential function that depends on L_{ww}:

$$f(r) = \exp\{-r/L_{ww}\} \tag{8}$$

and the value of L_{ww} can be inferred from the measured structure function $R_{ww}(\mathbf{x_0}, \mathbf{z})$ by fitting this exponential curve to the data. The integral length scale computed in this way depends on both horizontal and vertical positions; to remove the dependence on the horizontal position we have computed the streamwise averaged value of L_{ww}:

$$\langle L_{ww}(z)\rangle = \frac{1}{2H}\int_{-H}^{H} L_{ww}(x, z)\,\mathrm{d}x. \tag{9}$$

The vertical profiles of $\langle L_{ww}(z)\rangle$ for configurations A and B are plotted in Fig. 5a and for configurations A, C and D in Fig. 5b. The figures also provide an estimate of the uncertainty in the computed values of $\langle L_{ww}(z)\rangle$ due to both streamwise variations in $L_{ww}(z)$ and to experimental error in the individual measurements.

In configurations A and B, in the skimming flow regime, $\langle L_{ww}\rangle$ is essentially independent of the cavity geometry—the profiles are nearly identical, and the variations between the two are within the estimated uncertainty for the profiles (Fig. 5a). This clearly shows that, in skimming flow, the size of the turbulent eddies that develop close to the wall is limited by the horizontal spacing between the obstacles. Therefore when these are packed together sufficiently closely the obstacle height is not a characteristic length scale of the overlying boundary-layer flow. This result confirms previous findings from experimental (Perry et al. 1969) and numerical studies (Leonardi et al. 2007).

Conversely, the values of L_{ww} in configurations C and D, in wake interference flow, are both significantly different from those in configuration A and are characterized by a greater variability, especially in the lower part of the flow field. This fact shows that when the spacing significantly exceeds the obstacle height the vortices generated in the wakes of the obstacles have more time to grow and the depth of the roughness sub-layer therefore increases significantly compared with that observed in the skimming flow regime.

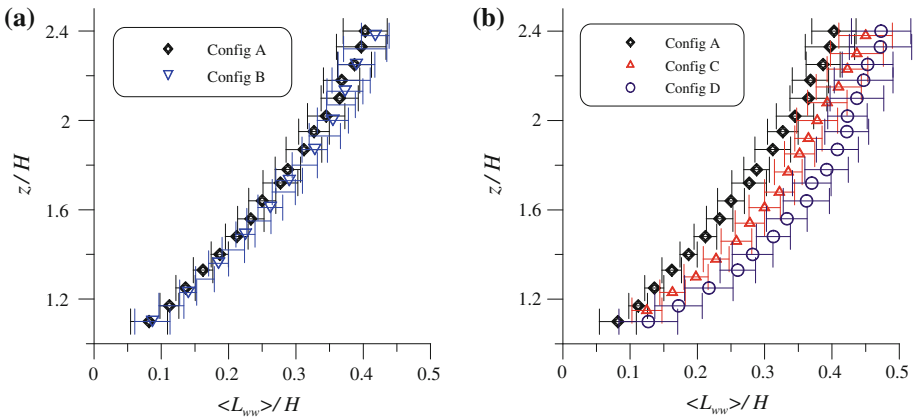

Fig. 5 Vertical profiles of the spatially-averaged integral length scale $\langle L_{\mathrm{ww}} \rangle$ of the vertical velocities for configurations A ($H/D = 1$), B ($H/D = 2/3$), C ($H/D = 1/2$) and D ($H/W = 1/3$); *error bars* give a measure the variability of L_{ww} along the streamwise axis x

4.2 Shear-Layer Flow

Shear at the interface between the cavity and the external generates a Kelvin–Helmholtz type instability in the layer, which can be clearly observed in Fig. 1. It is worth mentioning that these instabilities are strictly related to the two-dimensional structure of the flow field and could not be observed in experiments performed over three-dimensional canopies composed of a sparse group of obstacles (Huq et al. 2007). This flow is in many ways similar to a shear layer developing between two parallel flows. However there are also some important differences:

- The flow in the cavity is not always parallel to the external flow, and the velocity in the cavity varies with horizontal distance from the upwind corner.
- The mean velocities in the external flow vary rapidly with vertical distance from the shear layer.
- The turbulence intensity of the external flow $i(z) = \sqrt{\frac{1}{2}q(z)^2}/U(z)$ is of the same order as the turbulence levels in the shear layer, and is typically in the range $0.08 < i(z) < 0.16$.

As a result of these differences, the shear layer cannot be analyzed in the same way as for the canonical case. In particular, we cannot define the boundaries of the shear layer in terms of the mean velocities relative to the velocities outside the layer. Typically, in a mixing layer formed between two parallel uniform streams the outer edges may be defined as the points for which $U = \overline{U} \pm \alpha \Delta U$, where $\overline{U} = (U_1 + U_2)/2$, $\Delta U = U_1 - U_2$ and α is a constant taking values between 0.45 and 0.48. But in the mixing layer above a cavity the external flow is not uniform and the boundary-layer height is much greater than the depth of the cavity ($\delta \approx 10H$) so the velocity in the upper layer, just outside the shear layer, is very different from U_∞ and will depend on the local thickness of the shear layer; the velocity in the cavity varies with the horizontal distance from the upwind corner. To circumvent this problem we have defined the boundaries of the mixing layer in terms of the production of t.k.e. P, which we calculated as

$$P = \overline{u'u'}\frac{\partial \overline{u}}{\partial x} + \overline{u'w'}\frac{\partial \overline{u}}{\partial z} + \overline{w'u'}\frac{\partial \overline{w}}{\partial x} + \overline{w'w'}\frac{\partial \overline{w}}{\partial z}. \tag{10}$$

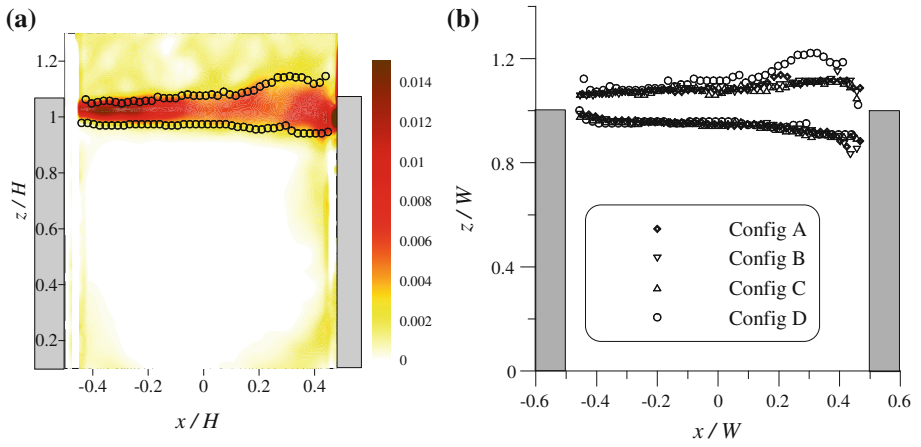

Fig. 6 **a** Normalized t.k.e. production PH/U_∞^3 for configuration D. **b** Shear-layer boundaries for the different configurations

As can be seen in Fig. 6a, the mixing layer is characterized by a very high level of t.k.e. production, which falls off very sharply at the outer edges of the layer. The boundaries can then be defined using a threshold value of the spatial derivative $\partial P/\partial z$. Figure 6b shows the shear-layer boundaries, computed for all configurations studied. It is worth noting that we could not detect significant variations in the shear-layer boundaries, from one configuration to another, except for the upper limit in configuration D. However those differences might be due to an artefact of the experiment, since the higher level of turbulence in the external flow blurs the boundary between the core of the shear layer and the external flow. Once the edges of the layer have been determined in this way, the velocity difference across the layer is defined from the velocities on the upper and the lower edges, at the centre of the cavity, i.e. $\Delta U = U_1(x = 0) - U_2(x = 0)$. The corresponding values for the four configurations are given in Table 1.[2]

We have used the definitions of the boundaries of the shear layer and the velocity difference ΔU to scale the velocity profiles at the top of the cavity. Figure 7 shows the vertical profiles of mean horizontal velocity $\overline{u}$, Reynolds stress and t.k.e. normalized by ΔU. The mean velocity profiles collapse onto a single curve, suggesting that this flow variable attains self-similarity. However, neither the Reynolds stress nor the t.k.e profile collapses onto a single curve. This means that ΔU cannot be the only relevant velocity scale in the shear layer and that the dynamics of the flow in that region are not entirely determined by the local t.k.e. production, as would be the case for a plane mixing layer. This suggests that the turbulent fluxes of t.k.e. have an important influence on the shear-layer dynamics. Indirect confirmation of the influence of t.k.e. fluxes arising from the external boundary-layer flow is given by the analysis of the velocity profiles normalized by u_*, the friction velocity of the overlying boundary-layer flow. These are shown in Fig. 8. This scaling clearly reduces the differences between the Reynolds stress profiles compared with the other scaling variables: we interpret this reduced variabilities as indicating the influence of the external flow conditions on the turbulent transfer within the shear layer.

[2] The values of ΔU differ from those presented in Salizzoni et al. (2009a) since the threshold for $\partial P/\partial z$ has been redefined. This difference however does not affect in any way the conclusions of this analysis.

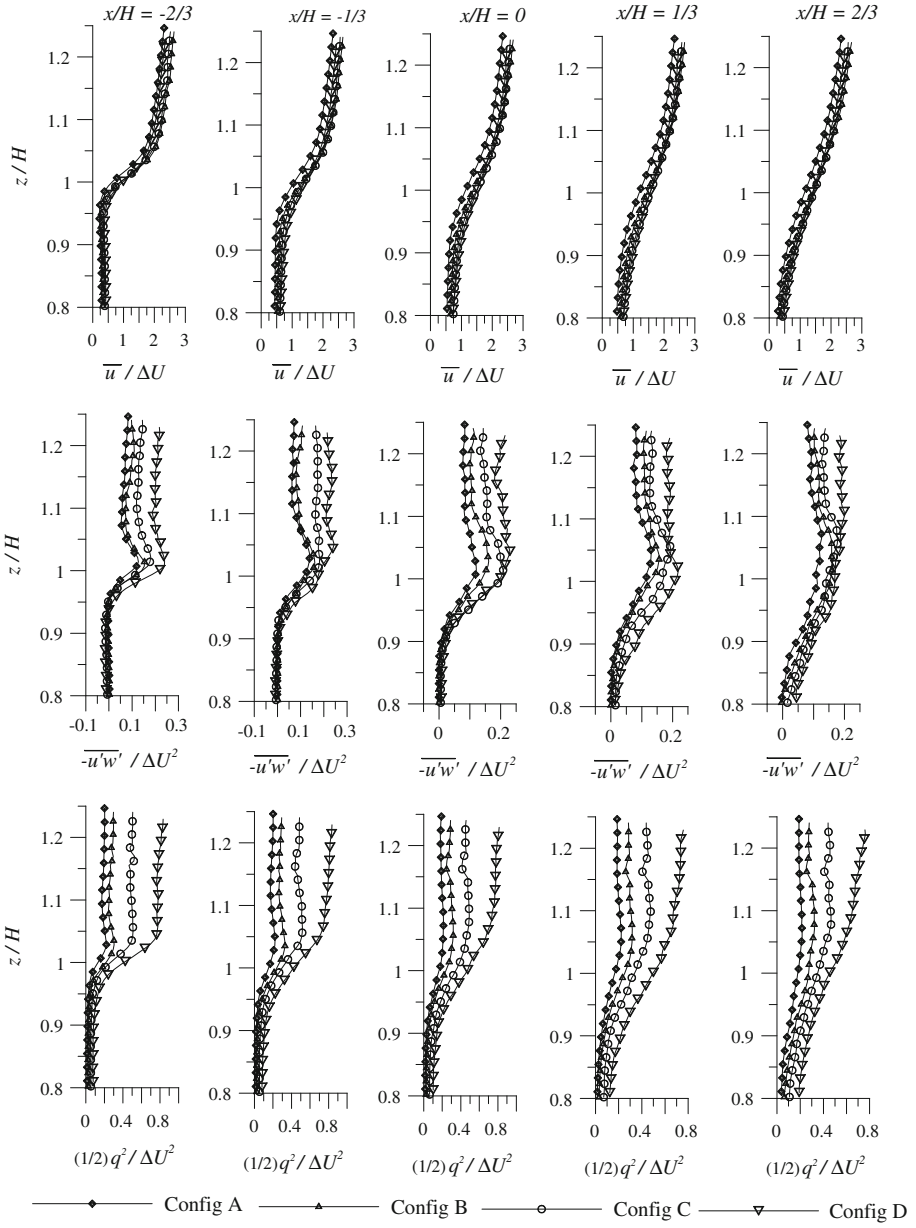

Fig. 7 Velocity, Reynolds stress and t.k.e. profiles in the shear layer at different streamwise locations x/H normalized with ΔU, the mean velocity difference at the top of the cavity

The profiles of t.k.e. normalized by u_* (Fig. 8) show that the t.k.e. outside the mixing layer (both in the cavity and in the overlying boundary layer) scales on u_* rather than on ΔU, for all four configurations. Within the mixing layer, however, the situation is more complex.

The t.k.e. profiles all show a systematic decrease across the mixing layer, from a high value outside the cavity to a low value within the cavity, and the region over which the t.k.e. varies

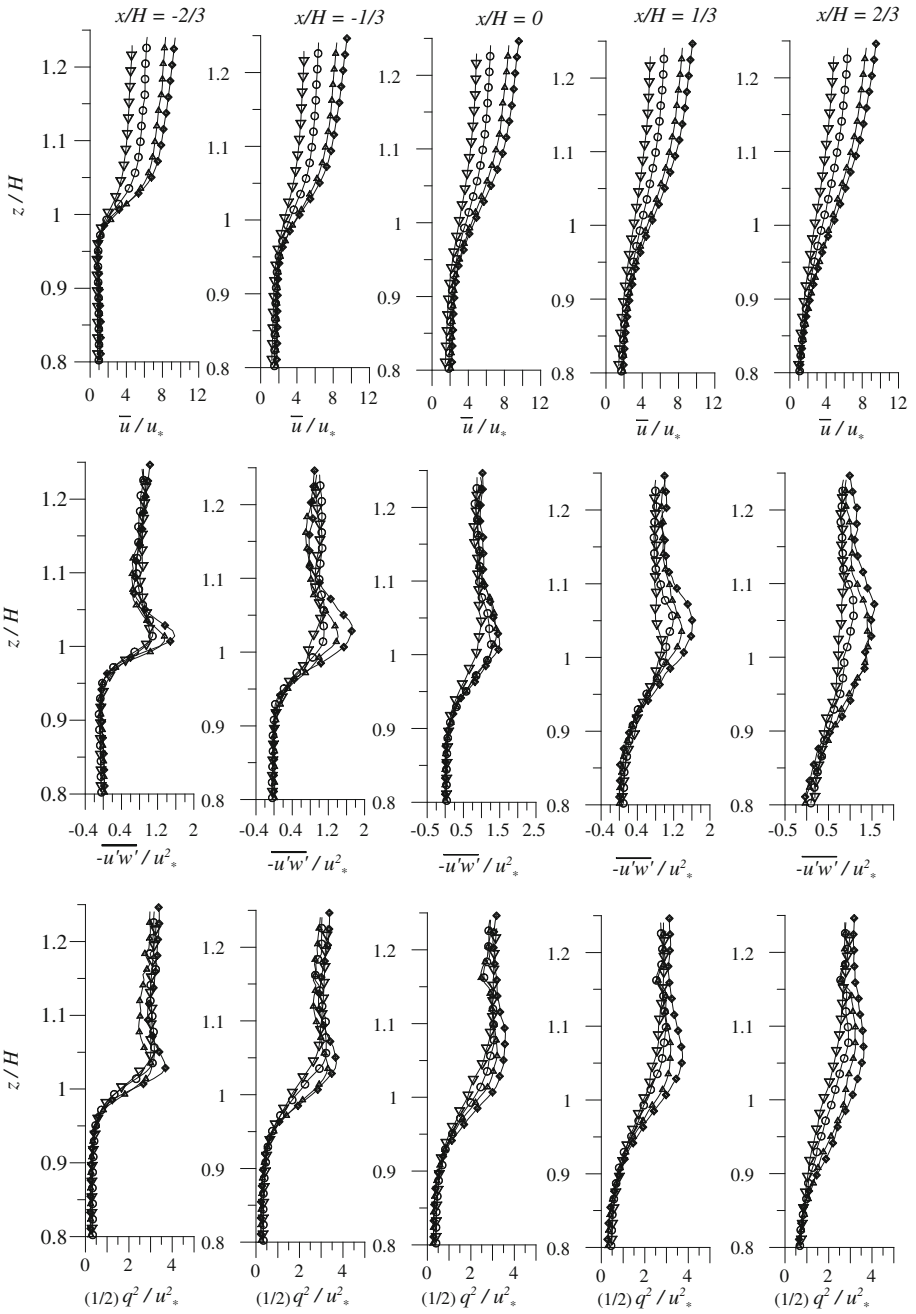

Fig. 8 Velocity, Reynolds stress and t.k.e. profiles in the shear layer at different streamwise locations x/H normalized with u_*, the friction velocity of the overlying boundary-layer flow. Same symbols as in Fig. 7

corresponds well with the boundaries of the mixing layer as determined from the production of t.k.e. The profiles therefore illustrate the diffusion of t.k.e. from the outer flow to the flow within the cavity. However the exact form of the t.k.e. profiles within the mixing layer varies

from one configuration to another, as can be seen in Figs. 7 and 8, and the profiles within the mixing layer do not really scale on either ΔU or u_*. The profiles for configurations A and B show a peak in the t.k.e. within the mixing layer, at all values of x/H indicating that additional t.k.e. is being generated by shear within the mixing layer. This peak occurs on the fast side of the mixing layer, as in conventional laboratory mixing layers. These two configurations have the lowest values of u_* and the highest values of ΔU, so it is plausible to conclude that the t.k.e. within the mixing layer is dominated by production from the shear across the mixing layer. This could explain why the two profiles do not scale on u_* within the mixing layer, but it is then surprising that they do not scale on ΔU either, since this scale ought to characterize the shear in the mixing layer. The profiles for configurations C and D are different from those for A and B, because they do not show any evidence of a peak in the t.k.e. within the mixing layer (this can be seen most clearly in Fig. 7). Configurations B and C both show a local decrease in the t.k.e. (at $z/H \approx 1.15$) but for all the profiles apart from that at $x/H = 2/3$ this point is well outside the mixing layer and so cannot be considered to indicate a local peak in the t.k.e. within the mixing layer (but we currently have no explanation for this local decrease in t.k.e.). Within the mixing layer, the profiles for configurations C and D do not collapse exactly when scaled on u_* but they do become very similar, especially when compared with the scaling on ΔU (Fig. 7), both inside and outside the mixing layer. Since these two configurations are those with the highest values of u_* and the lowest values of ΔU, it seems reasonable to conclude that, for these configurations, the diffusion of t.k.e. across the mixing layer dominates the production of t.k.e. within the layer. This would mean that there is some critical value of the ratio $\Delta U/u_*$ (between 2.48 and 3.27) that determines the relative importance of the production and diffusion processes for the t.k.e. profile within the mixing layer. It still remains to explain why the production-dominated profiles do not scale on ΔU.

Based on this analysis, we conclude that the mechanisms governing the flow dynamics are not similar to those observed in a planar mixing layer and that the flow in this region is directly influenced by the dynamics of the overlying boundary-layer flow.

4.3 Cavity Flow

Finally, we examine the flow within the cavity, beginning with possible scalings for the mean velocity, the Reynolds stress and the t.k.e. Horizontal and vertical profiles of mean velocity, measured at the centre of the cavity (i.e. along $z/H = 1/2$ and $x/H = 0$) are plotted in Fig. 9 normalized by U_∞ (Fig. 9a), ΔU (Fig. 9b) and u_* (Fig. 9c). As mentioned in Sect. 2 U_∞ is identical for all four configurations, therefore the profiles in Fig. 9a are directly representative of the raw data. The corresponding profiles of Reynolds stress are shown in Fig. 10a–c, and the profiles of t.k.e. are plotted in Fig. 11a–f (in this case horizontal and vertical profiles have been plotted separately, for clarity). Figure 9a shows surprisingly that the mean velocity within the canyon hardly varies in the four configurations studied. Given this condition it is evident that neither the velocity difference across the shear layer ΔU nor the friction velocity of the outer flow u_* is an appropriate scale for the mean velocities within the canyon (Fig. 9b, c). This is also true for the Reynolds stress (Fig. 10a–c), although the differences between the possible scalings are less evident than for the mean velocities since the values are close to zero in most of the canyon. On the other hand, the t.k.e. (Fig. 11a–f) appears to scale best on the friction velocity of the outer flow. This apparent scaling of the mean velocities on U_∞ is surprising, given that the conditions in the boundary layer vary significantly in the four configurations, so that U_∞ is not particularly representative of the velocities at the bottom of the boundary layer.

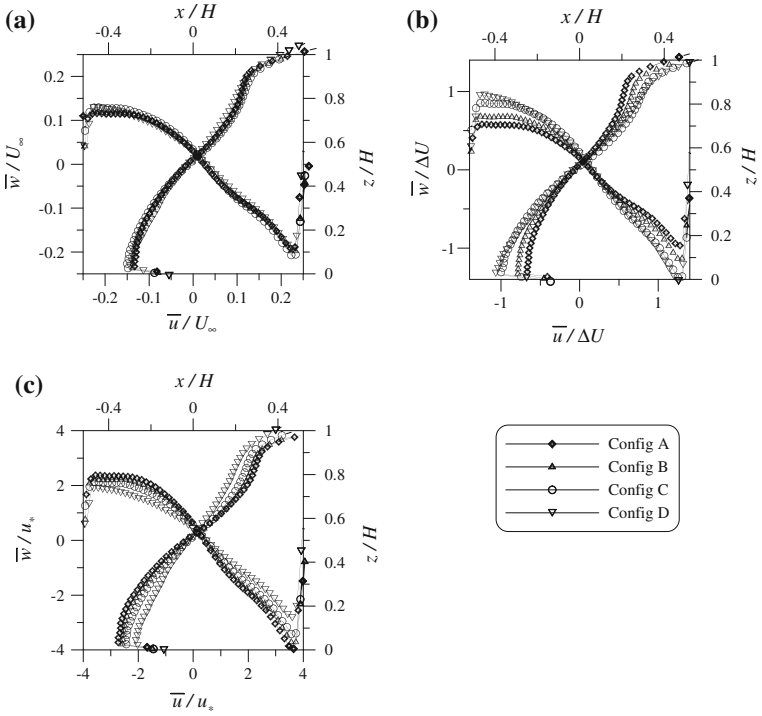

Fig. 9 Mean velocity profiles within the cavity normalized with **a** U_∞, **b** ΔU and **c** u_*. Vertical profiles of horizontal mean velocity $\overline{u}$ are at $x = 0$ and horizontal profiles of vertical mean velocity $\overline{w}$ are at $z = H/2$

Figure 9 show that the maximum downward mean vertical velocity on the centreline ($z/H = 1/2$) is almost the same as the peak horizontal velocity at the top of the cavity, at $x/H = 0$ ($\overline{u}/U_\infty \approx \overline{w}/U_\infty \approx 0.25$), but the peak in the vertical velocity is displaced away from the cavity wall by the growth of the boundary layer. At the centre of the cavity the velocity profiles are close to linear with a constant gradient whereas the slope of the velocity profile decreases as the wall is approached. This effect is then cancelled out at the upper interface of the cavity by the acceleration provided by the outer flow, across the shear layer. The profiles of Reynolds stress (Fig. 10a–c) show much less variability between the four configurations, irrespective of scaling, and this is principally because the values are close to zero almost everywhere except in the shear layer and close to the cavity walls. In these regions, the Reynolds stress also appears to scale most satisfactorily on the far field velocity U_∞. The shear in the interface layer at the top of the cavity induces very high Reynolds stresses, which decay as the fluid is transported around the cavity; at the mid-point on the downwind wall of the cavity the level has decreased to about 1/4 of the level in the shear layer.

The vertical and horizontal profiles of t.k.e. show that the t.k.e. for the four configurations scales on the friction velocity u_*, rather than on ΔU (Fig. 11a–f). This suggests that the dynamics of the t.k.e. are dominated by the turbulence entrained from the external flow, which is then transported through the cavity by the mean flow. The maximum t.k.e. levels at the centre of the interface are of the same order as those at the centre of the downwind face ($(1/2)q^2/u_*^2 \approx 1.6$) but the t.k.e. then decays very rapidly as it is transported round the

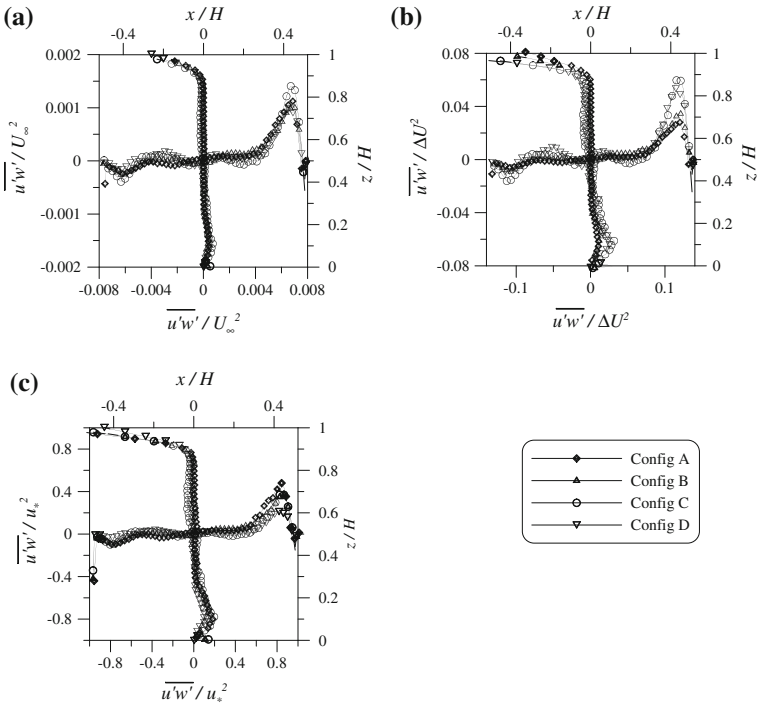

Fig. 10 Reynolds-stress profiles within the cavity normalized with **a** U_∞, **b** ΔU and **c** u_*.Vertical profiles are at $x = 0$ and horizontal profiles are at $z = H/2$

cavity; at the centre of the cavity floor it has fallen to about half of its maximum value at the top of the cavity.

The reduced scatter in the t.k.e. profiles normalized by the friction velocity u_* has important implications for parametric models of the turbulent transfer between the canyon and the external flow. Experimental results of pollutant exchange velocities from the cavity, referred to as u_d, measured in the same configurations discussed here (Salizzoni et al. 2009b) showed that the wash-out process is mainly governed by the intensity of the fluctuating velocities within the cavity, and hence on the t.k.e. levels. Since these scale on u_* we expect that the transfer velocities u_d scale on u_* too. This is confirmed by the results presented in Table 2 where we show that non-dimensional transfer velocities u_d/u_* tend to an almost constant value.

Concerning the nature of flow dynamics within the cavity it is interesting to note, as shown in Figs. 10 and 11, that the t.k.e. field within the cavity is decoupled from the Reynolds-stress distribution, i.e. higher values of t.k.e. do not correspond to higher values of Reynolds stress. This implies that the 'effectiveness' of the turbulent transfer of momentum is not related to the intensity of the velocity fluctuations. This further implies that the flows within the canyon that occur in the four different configurations are not dynamically similar, even if they are taking place in a geometrically similar domain. It is possible that the t.k.e. levels within the cavity are due to the action of 'inactive' swirling structures, i.e. eddies that do not contribute to momentum transfer.

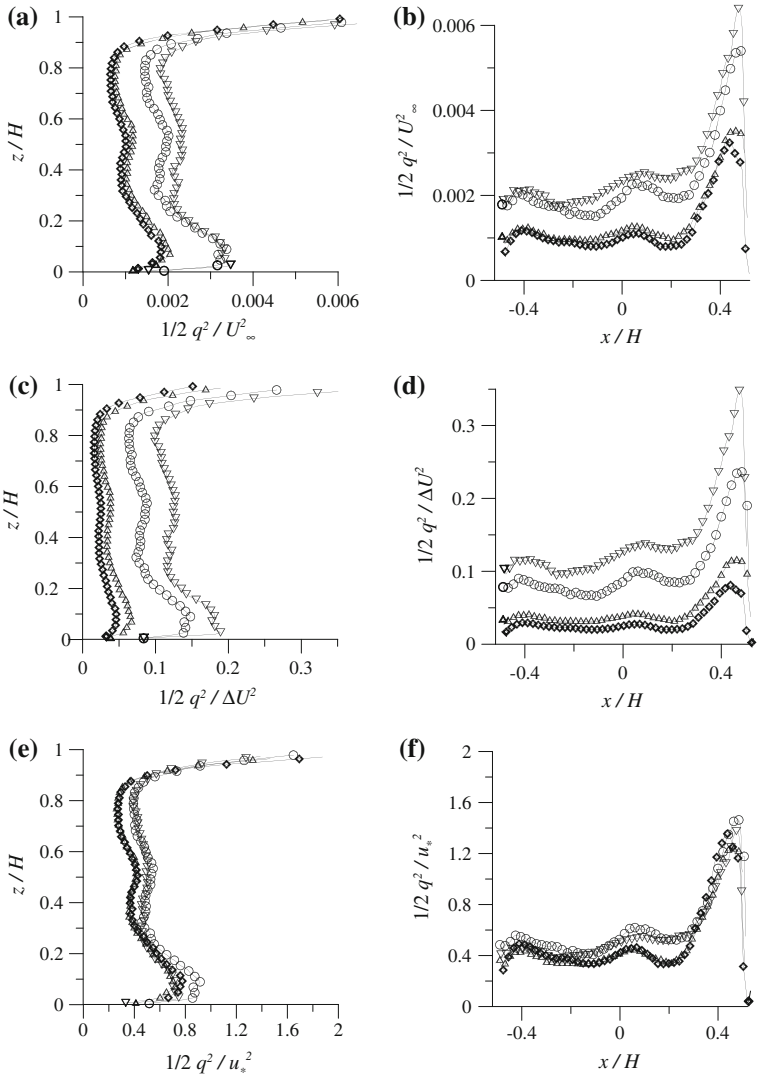

Fig. 11 Vertical and horizontal profiles of t.k.e. profiles within the cavity normalized with U_∞ (**a** and **b**), ΔU (**c** and **d**) and u_* (**e** and **f**). Same symbols as in Fig. 10

Table 2 Mass transfer velocities u_d from the canyon to the external flow

Configuration	H/D	u_* (m s^{-1})	u_d (m s^{-1})	u_d/u_*
A	1	0.33	0.066	0.200
B	2/3	0.36	0.073	0.202
C	1/2	0.41	0.076	0.185
D	1/3	0.46	0.78	0.171

Experimental results from Salizzoni et al. (2009b)

The fact that the t.k.e. fluxes scale on u_* and the Reynolds stresses are close to zero almost everywhere in the cavity shows that the turbulent fluctuations are associated with unsteady structures that do not make any net contribution to momentum transfer. There are two possible explanations for this, depending on whether the turbulent fluctuations are generated by small-scale structures or large-scale structures. If the turbulent fluctuations are generated by small-scale structures in the flow, then these structures have to exhibit some form of symmetry in their geometrical structure; something similar to this is observed in homogeneous isotropic turbulence, where the symmetry of the vortical structures creates turbulence in which the net Reynolds stress is equal to zero. In the cavity flow studied here, these small-scale structures would have to be entrained into the cavity from the external flow by the flapping of the shear layer, but the turbulence in the boundary layer above the mixing layer is far from being homogeneous and isotropic (Sect. 4.1), so it is also necessary to explain how the small-scale structures that are entrained become isotropic. There are two possible mechanisms:

– Whilst being transported across the mixing layer the small-scale structures are stretched and deformed by the shear so that they lose their initial topological characteristics, becoming isotropic.
– Only the smaller scale structures are entrained by the mixing layer, and these lie within the inertial range of the external flow, so they are already close to being symmetrical.

If, on the other hand, the turbulent fluctuations in the cavity are generated by large-scale structures then it is possible that these are caused by fluctuations involving the whole body of fluid in the cavity, in a coherent rotating motion. A similar phenomenon was identified by Townsend (1976) in turbulent boundary layers, where flows with similar values of u_* could exhibit different profiles of turbulent intensity $i = \sigma_u/U$. He suggested that "…large-scale swirling in planes parallel to the wall [that] do not extract energy from the mean flow or affect the rate of energy transfer to smaller eddies for viscous dissipation. Swirling motions contribute little to Reynolds stress, and their effect on that part of the layer between the point of observation and the wall is one of slow random variations of 'mean velocity' which cause corresponding variations of wall stress. It is possible and useful to regard the 'swirl' component of local motion as an *inactive* component which may be ignored in any discussion of the local flow …" (Townsend 1976, pp. 153–154). Similarly, in the flow studied here, it is possible that the t.k.e. depends at least partially on fluctuations involving the whole body of fluid within the cavity in a coherent rotating motion. In order to test these hypotheses we have analyzed the flow structure within the canyon.

4.3.1 Flow Structure

In the previous paragraph we showed the influence of the intensity of the external turbulence on the turbulent motion within the cavity. Similarly, we may expect the flow structure within the cavity to be influenced by the structure of the external turbulence.

To study this dependence we computed the auto-correlation coefficients R_{uu} and R_{ww} over the entire domain and we have evaluated the functions $L_{uu}(x, z)$ and $L_{ww}(x, z)$ (Sect. 4.1) within the cavity. These are shown in Fig. 12. For two of the profiles (Fig. 12b, c), higher values of L_{ww} are detected close to the vertical walls whereas L_{uu} increases close to the bottom of the cavity. To explain the behaviour of L_{uu} and L_{ww} we turn to the spatial distribution of the r.m.s. (σ_u, σ_w) of the horizontal and vertical velocities within the cavity. These are shown in Fig. 13.

The graph of σ_u/U_∞ (Fig. 13a) shows clearly how turbulent fluid is entrained into the cavity at the upper downwind corner, and as the fluid is transported round the cavity the

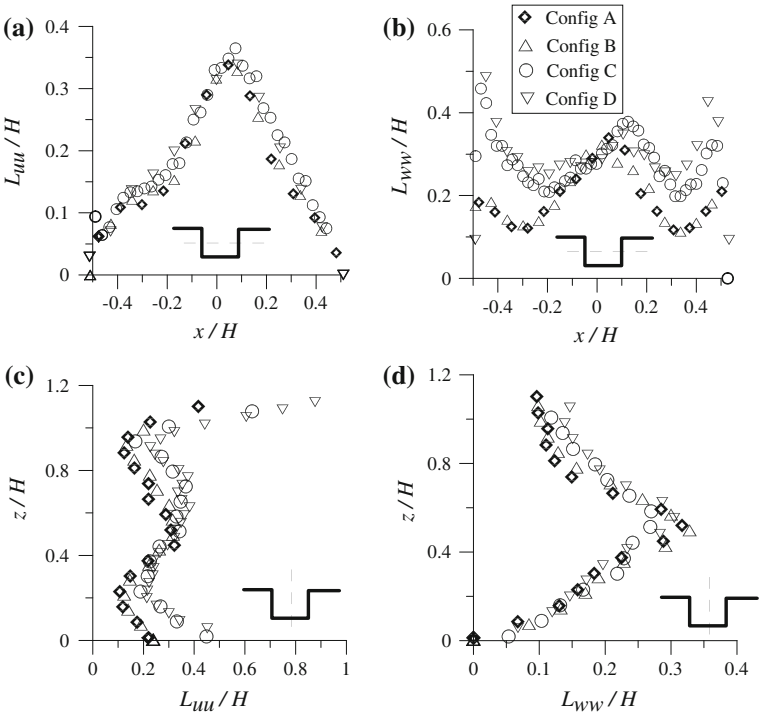

Fig. 12 Evaluation of the maximum integral length scales L_{uu} and L_{ww} within a square cavity for the different configurations. **a** and **b** show horizontal profiles at mid height (i.e. $z/H = 1/2$) for L_{uu} and L_{ww} respectively; **c** and **d** show vertical profiles at the centre of the cavity (i.e. $x/H = 0$) of L_{uu} and L_{ww} respectively

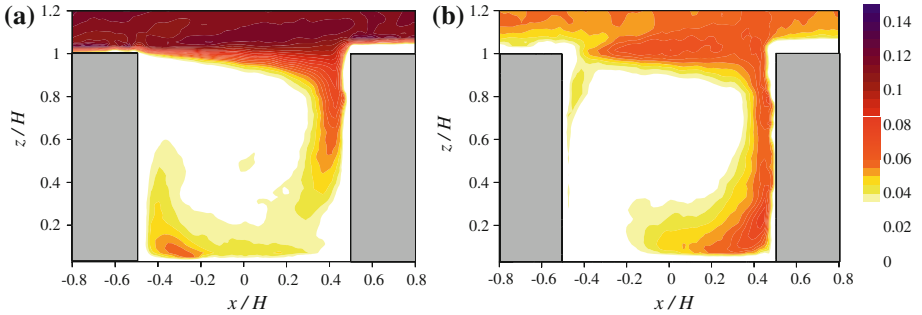

Fig. 13 Normalized r.m.s. values of **a** horizontal σ_u/U_∞ and **b** vertical velocity fluctuation σ_w/U_∞ within the cavity

horizontal fluctuations first decay and then grow again as the fluid moves parallel to the bottom of the cavity, reaching a maximum at the lower upwind corner of the cavity. This decrease and subsequent increase in the horizontal velocity fluctuations indicates that the turbulence is not only caused by the entrainment of turbulent structures from outside the cavity, but must also be the result of turbulence generation within the cavity, and modification of that turbulence by interaction with the walls of the cavity. In the first part of the flow, parallel to the downwind vertical cavity wall, the horizontal fluctuations are damped by the

presence of the vertical wall and part of the energy is transmitted to fluctuations in the plane parallel to the wall (σ_v and σ_w) by the blocking effect of the wall (as discussed, for example, in Bearman 1972 and Hunt et al. 1990). As the flow advances along the bottom of the cavity the velocity fluctuations perpendicular to the wall are damped out rather rapidly (Fig. 13b) whilst the horizontal fluctuations increase, due both to the blocking effect of the floor on the vertical fluctuations and to shear generated by the rigid boundary. The blocking effect of the upwind wall in the cavity amplifies the turbulent fluctuations in the approaching flow, and as a result there is a local maximum in the horizontal fluctuations close to the lower downwind corner of the cavity. So, the differences in the general behaviour of the functions L_{uu} and L_{ww} can be interpreted as the effect of a plane rigid boundary on the structure of the flow, increasing the correlations between the velocity components in the directions parallel to the wall.

In these regions we observe also that the values of L_{uu} and L_{ww} for configurations C and D are generally higher than those for configurations A and B. This shows that, in general, increased velocity correlations in the external flow are associated with higher velocity correlations within the cavity for both the horizontal and the vertical components of the velocity field. This result tends to support the hypothesis that the increased levels of t.k.e. within the cavity are essentially related to larger scale velocity fluctuations.

5 Conclusions

The influence of external flow conditions on the transfer of momentum between an idealized street canyon and the overlying boundary layer has been investigated experimentally using PIV and HWA to measure the velocity fields inside and above the canyon. The results show that momentum transfer is due essentially to a coupling between the turbulent structures in the outer flow and the structures in the shear-layer interface between the two regions. The main features of this interaction are:

1. The dynamics of the shear layer flow at the top of the canyon are significantly influenced by turbulent t.k.e. fluxes from the external flow.
2. The flow within the cavity depends on turbulent t.k.e. fluxes from the external flow.
3. The structure of the flow within the cavity is sensitive to changes in the structure of the external flow.
4. The turbulent velocity fluctuations within the cavity are mainly due to larger scale fluctuations.
5. The transfer process cannot be rigorously expressed in a non-dimensional form based on a single velocity scale.

The results from the experiments reported herein show that the interaction between the shear layer and the overlying flow is complex, involving several different physical mechanisms, and that as a result there is no single velocity scale that characterizes all aspects of the flow. Some processes scale on the friction velocity of the overlying flow, whilst others scale on the velocity difference between the external flow and the flow in the cavity. And although the flow in the cavity is driven by the external flow, the velocity difference across the interface does not scale on the friction velocity. This means that the first two scaling hypotheses developed at the outset (Eqs. 1 and 2) are not confirmed, but the data are consistent with the third hypothesis (Eq. 3c). More work is still required on the exact relationship between the outer flow and the velocity difference across the interface, since this clearly depends on a number of independent physical parameters that characterize the cavity and the boundary conditions

upstream of the cavity. This has important implications for the definition of parametric relationships for the turbulent exchange of material in the urban canopy, since these relationships will need to take into account both local conditions and conditions upwind of the street canyons—in other words, any simple model for an inhomogeneous urban surface will have to take into account wind direction, since this will determine the properties of the incident wind. The results presented here concern essentially two-dimensional configurations, whereas, in reality, all streets are of finite length, and are not necessarily oriented perpendicular to the wind. The general problem of flow and dispersion in a finite length street canyon for arbitrary wind direction was studied by Soulhac et al. (2008). They showed that, in the central section of the street, certain aspects of the flow could be derived from a suitable linear superposition of the flow perpendicular to the street and the flow along the street, and that where there was coupling between the two components, the transverse component modified the longitudinal component, but was itself essentially unmodified. A companion study of flow and dispersion in street intersections (Soulhac et al. 2009) showed that the influence of a street intersection extends into the adjoining streets to a distance approximately equal to the characteristic scale of the streets, so it is likely that the results presented herein will remain applicable in urban environments characterized by relatively long streets in grid patterns (as studied, for example, by Garbero et al. 2010). However the flow structure in a sparse obstacle array is likely to be very different; Huq et al. (2007) for example, did not detect any clear sign of Kelvin–Helmholtz type shear-layer instabilities in their experimental study of flow in an urban canopy characterized by large 3D obstacles. In such a configuration the recirculation patterns are considerably more complicated, and strongly three-dimensional, so we would not expect the scalings developed here to be applicable to urban canopies with those characteristics.

Acknowledgments The authors would like to thank one of the anonymous referees for drawing their attention to the differences in the turbulent kinetic energy profiles for the four configurations.

References

Bearman P (1972) Some measurements of the distortion of turbulence approaching a two-dimensional bluff body. J Fluid Mech 53(3):451–467

Belcher SE (2005) Mixing and transport in urban areas. Philos Trans Roy Soc 363:2947–2963

Castelain T (2006) Contrôle de jet par microjets impactants. Ph.D. thesis, Ecole Centrale de Lyon, 173 pp

Caton F, Britter R, Dalziel S (2003) Dispersion mechanism in a street canyon. Atmos Environ 37:693–702

Coceal O, Belcher SE (2004) A canopy model of mean winds through urban areas. Q J Roy Meteorol Soc 130:1349–1372

Coceal O, Thomas TG, Castro IP, Belcher SE (2006) Mean flow and turbulence statistics over groups of urban-like obstacles. Boundary-Layer Meteorol 121:491–519

Coceal O, Dobre A, Thomas TG (2007) Unsteady dynamics and organized structures from DNS over an idealized building canopy. Int J Climatol 27:1943–1953

Finnigan JJ (1985) Turbulent transport in flexible plant canopies. In: Hutchinson B, Hicks B (eds) The forest–atmosphere interaction. D. Reidel Publishing Co., Dordrecht, pp 443–480

Finnigan JJ (2000) Turbulence in plant canopies. Annu Rev Fluid Mech 32:519–572

Fouras A, Soria J (1998) Accuracy of out-of-plane vorticity measurements derived from in-plane velocity field data. Exp Fluids 25:409–430

Garbero V, Salizzoni P, Soulhac L (2010) Experimental study of pollutant dispersion within a network of streets. Boundary-Layer Meteorol 136:457–487

Grimmond CSB, Oke TR (1999) Aerodynamic properties of urban areas derived from analysis of surface form. J Appl Meteorol 38:1262–1292

Hamlyn D, Hilderman T, Britter R (2007) A simple network approach to modelling dispersion among large groups of obstacles. Atmos Environ 41(28):5848–5862

Harman IN, Belcher SE (2006) The surface energy balance and boundary layer over urban street canyons. Q J Roy Meteorol Soc 132:2749–2768

Hunt J, Kawai H, Ramsay S, Pedrizetti G, Perkins R (1990) A review of velocity and pressure fluctuations in turbulent flows around bluff bodies. J Wind Eng Ind Aerodyn 35:49–85

Huq P, Carrillo A, White LA, Redondo J, Dharmavaram S, Hanna SR (2007) The shear layer above and in urban canopies. J Appl Meteorol Climatol 46:368–376

Irwin HP (1981) The design of spires for wind simulation. J Wind Eng Ind Aerodyn 7:361–366

Jimènez J (2004) Turbulent flows over rough wall. Annu Rev Fluid Mech 36:96–173

Kaimal J, Finnigan J (1994) Atmospheric boundary layer flow. Oxford University Press, New York, 289 pp

Kim J, Baik J (2003) Effects of inflow turbulence intensity on flow and pollutant dispersion in an urban street canyon. J Wind Eng Ind Aerodyn 91:309–329

Leonardi S, Orlandi P, Antonia R (2007) Properties of d- and k-type roughness in a turbulent channel. Phys Fluids 19:125101

Louka P, Belcher SE, Harrison RG (2000) Coupling between air flow in streets and the well-developed boundary-layer aloft. Atmos Environ 34(16):2613–2622

Perry A, Shofield WH, Joubert PN (1969) Rough wall turbulent boundary layers. J Fluid Mech 37:383–413

Poggi D, Katul GC (2007) Turbulent flows on forested hilly terrain: the recirculation region. Q J Roy Meteorol Soc 133:1027–1039

Raupach MR, Antonia R, Rajagopalan S (1991) Rough-wall turbulent boundary layers. Appl Mech Rev 44(1):1–25

Salizzoni P, Soulhac L, Mejean P, Perkins R (2008) Influence of a two scale surface roughness on a turbulent boundary layer. Boundary-Layer Meteorol 127(1):97–110

Salizzoni P, Soulhac L, Mejean P (2009a) Street canyon ventilation and atmospheric turbulence. Atmos Environ 43:5056–5067

Salizzoni P, Van Liefferinge R, Soulhac L, Mejean P, Perkins RJ (2009b) Influence of wall roughness on the dispersion of a passive scalar in a turbulent boundary layer. Atmos Environ 43(3):734–748

Salizzoni P, Van Liefferinge R, Mejean P, Soulhac L, Perkins RJ (2010) Scaling of the vertical spreading of a plume of a passive tracer in a rough-wall neutral boundary-layer. Boundary-Layer Meteorol 135:455–467

Simoëns S, Ayrault M, Wallace JM (2007) The flow across a street canyon with variable width—part 1: kinematic description. Atmos Environ 41:9002–9017

Soulhac L (2000) Modélisation de la dispersion atmosphérique à l'intérieur de la canopée urbaine. Ph.D. thesis, Ecole Centrale de Lyon, 345 pp

Soulhac L, Puel C, Duclaux O, Perkins R (2003) Simulations of atmospheric pollution in Greater Lyon an example of the use of nested models. Atmos Environ 37:5147–5156

Soulhac L, Perkins R, Salizzoni P (2008) Flow in a street canyon for any external wind direction. Boundary-Layer Meteorol 126:365–388

Soulhac L, Garbero V, Salizzoni P, Mejean P, Perkins R (2009) Flow and dispersion in street intersections. Atmos Environ 43:2981–2996

Stanislas M, Carlier J, Foucaut J, Dupont P (1998) Experimental study of a high Reynolds number turbulent boundary layer using DPIV. In: 9th International symposium on application of laser technology to fluid mechanics, Lisbon, Portugal

Townsend AA (1976) The structure of turbulent shear flows. Cambridge University Press, Cambridge, 444 pp